Journal of Materials Chemistry C

PAPER

View Article Online
View Journal | View Issue

Cite this: J. Mater. Chem. C, 2015, 3, 3694

Efficient OLEDs with low efficiency roll-off using iridium complexes possessing good electron mobility†

Qiu-Lei Xu, Xiao Liang, Song Zhang, Yi-Ming Jing, Xuan Liu, Guang-Zhao Lu, You-Xuan Zheng* and Jing-Lin Zuo

Received 9th January 2015,
Accepted 15th February 2015

DOI: 10.1039/c5tc00073d

www.rsc.org/MaterialsC

Two bis-cyclometalated iridium complexes (**Ir1** and **Ir2**) with trifluoromethyl substituted bipyridine (2′,6′-bis-(trifluoromethyl)-2,3′-bipyridine (**L1**) and 2′,6′-bis(trifluoromethyl)-2,4′-bipyridine (**L2**)) as the main ligands and tetraphenylimidodiphosphinate as the ancillary ligand were prepared, and their X-ray crystallography, photoluminescence, electrochemistry properties were investigated. The **Ir1** and **Ir2** complexes show green emissions at about 500 and 502 nm with high quantum efficiencies of 0.63 and 0.93, respectively. Moreover, they also exhibit higher electron mobility than that of Alq_3 (tris-(8-hydroxyquinoline)aluminium). The organic light emitting diodes (OLEDs) with the structure of ITO/TAPC (1,1-bis[4-(di-*p*-tolylamino)-phenyl]cyclohexane, 40 nm)/mCP (1,3-bis(9*H*-carbazol-9-yl)benzene, 10 nm)/Ir complex (8 wt%): PPO21 (3-(diphenylphosphoryl)-9-(4-(diphenylphosphoryl)phenyl)-9*H*-carbazole, 25 nm)/TmPyPB (1,3,5-tri(*m*-pyrid-3-yl-phenyl)benzene, 50 nm)/LiF (1 nm)/Al (100 nm) showed excellent performances, partly due to their high quantum efficiency and high electron mobility. For the devices **G1** and **G2**, the maximum current efficiency (η_c) values are as high as 101.96/99.97 cd A^{-1} and the maximum external quantum efficiencies of 31.6% and 30.5% with low electroluminescence efficiency roll-off. The η_c data still remain over 90 cd A^{-1} even at the luminance of 10 000 cd m^{-2}, which proves that the complexes have potential applications as efficient green emitters in OLEDs.

Introduction

Due to the high quantum efficiency, short lifetime of triplet excited states and broad range of emission colors, phosphorescent iridium(III) complexes have been widely used as dopants in organic light-emitting diodes (OLEDs).[1] The strong spin–orbit coupling (SOC) introduced by the central heavy atom can promote the triplet to ground radiative transition, resulting in unusually high phosphorescence quantum yields at room temperature. On the other hand, since the phosphorescence of Ir(III) complexes primarily originates from the metal-to-ligand charge transfers (MLCT) and the ligand-centered (LC) transitions,[1a] the energy level of the excited state can be controlled by tuning the energy levels of the ligands through substituent effects, which leads to a wide flexible emission color range.

However, for many OLEDs with high efficiency based on Ir(III) complexes, the device efficiency roll-off ratios are serious, which can mainly be attributed to the deterioration of charge carrier balance and the increase of nonradioactive quenching processes, including triplet–triplet annihilation (TTA), triplet-polaron annihilation (TPA), and electric field induced dissociation of excitons at high current density.[2] Therefore, the balanced injection and transport of the electron–hole is a crucial factor for high efficient OLEDs. As we know, because the hole mobility of most hole transport materials is roughly 2–3 orders of magnitude higher than the electron mobility of the electron transport materials, the efficiency and efficiency roll-off of OLEDs rely on the capability of electron transport. Thus, it is necessary to use the ambipolar host materials and synthesize Ir(III) dopants with outstanding electron mobility[3] to obtain phosphorescent OLEDs with low efficiency roll-off.

It is well-known that $Ph_2P{=}O$ has been widely used to construct electron transport and ambipolar host materials because of its ability to improve electron injecting and transporting capabilities due to its strongly electron-deficient nature.[4] In our group, we found that tetraphenylimidodiphosphinate (tpip) derivatives,[5]

State Key Laboratory of Coordination Chemistry, Collaborative Innovation Center of Advanced Microstructures, School of Chemistry and Chemical Engineering, Nanjing University, Nanjing 210093, P. R. China. E-mail: yxzheng@nju.edu.cn

† Electronic supplementary information (ESI) available: For the the ORTEP diagrams of **L2**, the crystallographic data for **L1**, **Ir1** and **Ir2**, the orbital distributions of complexes **Ir1**, **Ir2**, **IrA** and **IrB**, the transient EL signals for the device based on **Ir1**, the lifetime curves and normalized emission spectra of **Ir1** and **Ir2** in degassed solution. CCDC 996478–996480. For ESI and crystallographic data in CIF or other electronic format see DOI: 10.1039/c5tc00073d

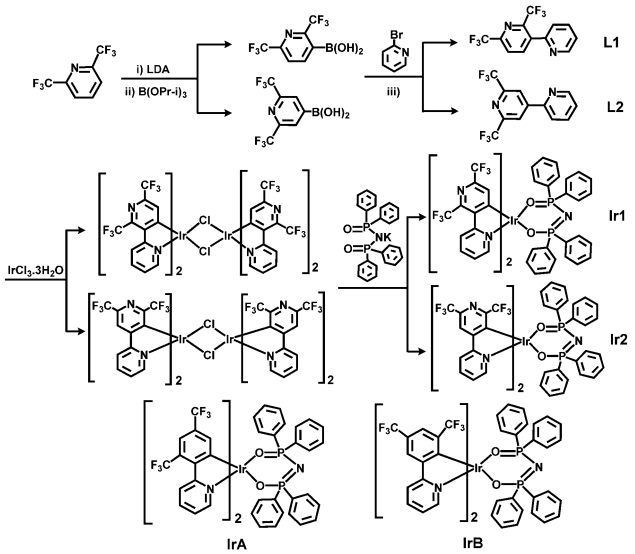

Scheme 1 Synthetic routes of ligands and complexes.

which have two diphenyl phosphoryl ($Ph_2P{=}O$) groups, are actually useful ancillary ligands for Ir(III) complexes and corresponding devices. Besides, Htpip has four bulky aromatic groups, which may lead to a larger spatial separation of the neighboring molecules of the Ir(III) complexes to suppress the TTA and TPA effectively. Moreover, fluorination can enhance the electron mobility and result in a better balance of charge injection and transfer, the lower vibrational frequency of the C–F bond can reduce the rate of radiationless deactivation, the bulky CF_3 substituents can affect the molecular packing and the steric protection around the metal can suppress the self-quenching behavior.[6] In addition, nitrogen heterocycle will increase the electron affinity and a more negative framework of ligand C^N such as bipyridine may improve the electron mobility. Thus, in this article we synthesized two iridium complexes (**Ir1** and **Ir2**, Scheme 1) with $-CF_3$ substituted bipyridine as the main ligand and tpip as the ancillary ligand, expecting to get efficient phosphorescent Ir(III) complexes with high electron mobility for high efficient OLEDs. To study the influence of introducing the bipyridine ligand on the properties of iridium complexes, we set our former reported $-CF_3$ substituted phenylpyridine complexes (**IrA** and **IrB**, Scheme 1) as references.[5c]

Results and discussion

Preparation and characterization of compounds

Scheme 1 shows the synthetic routes for the new iridium complexes **Ir1** and **Ir2**. The reaction of 2,6-bis(trifluoromethyl)-pyridine with LDA (lithium diisopropylamide) and $B(OPr\text{-}i)_3$ gave two crude aryl boronic acids. The corresponding two trifluoromethyl fluorinated bipyridine ligands (**L1** and **L2**) were synthesized using a Suzuki coupling reaction. The tetraphenyl-imidodiphosphinate acid (Htpip) and potassium salt (Ktpip) were prepared according to our previous publications.[5] The iridium complexes were obtained in two steps. The purification

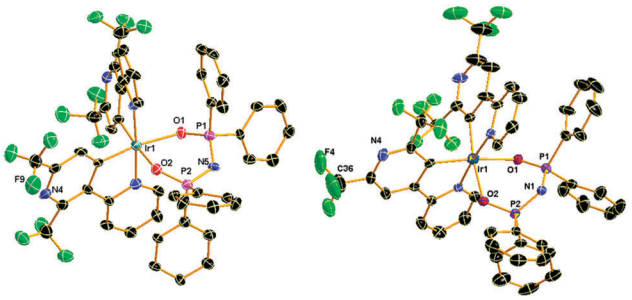

Fig. 1 Oak Ridge thermal ellipsoidal plot (ORTEP) diagrams of the complexes **Ir1** (left) and **Ir2** (right) with the atom-numbering schemes. Hydrogen atoms are omitted for clarity. Ellipsoids are drawn at 30% probability level.

of the mixture by silica chromatography provided the products **Ir1** and **Ir2**, which were further purified by vacuum sublimation. All the new compounds were fully characterized by ^{1}H NMR and high resolution mass spectrometry; moreover, the crystal structures further confirmed the identity of both the complexes.

X-ray crystallography

Single crystals of **L1** (Fig. S1, ESI†) and **Ir2** were obtained from petroleum ether and CH_2Cl_2 solutions, and **Ir1** was grown from vacuum sublimation. Fig. 1 shows the Oak Ridge thermal ellipsoidal plot (ORTEP)[7] diagrams of **Ir1** and **Ir2** given by X-ray analysis. The selected parameters of the molecular structures and atomic coordinates were collected in the Tables S1 and S2 (ESI†). The iridium center adopts a distorted octahedral coordination geometry with two C^N cyclometalated ligands and one O^O ancillary ligand. For the **Ir1**, the range of dihedral angles between two pyridine rings of each ligand are 7.3(9)–19.3°, indicating that the two pyridine ring are not coplanar for the steric effect of the trifluoromethyl group. The Ir–N bond lengths ranging from 2.004(6) to 2.006(5) Å and Ir–C bond length ranging from 1.868(7) to 1.977(6) Å are slightly shorter than values reported for **IrA** (Ir–N = 2.016(3)–2.025(4) Å and Ir–C = 1.974(9)–1.981(8) Å). The bond length ranges of Ir–N and Ir–C in **Ir2** are 2.031(8)–2.061(8) Å and 2.012(9)–2.039(9) Å, respectively. Furthermore, the C–C and C–N bond lengths and angles are in agreement with the corresponding parameters described in other similarly constituted complexes.

Thermal stability

The thermal stability of emitters is very important for efficient OLEDs. If a complex is suitable for application in OLEDs, the melting point (T_m) and decomposition temperature (T_d) should be high enough to guarantee that the complex could be deposited onto the solid face without any decomposition on sublimation. The differential scanning calorimetry (DSC) and thermogravimetric analysis (TGA) curves of **Ir1** and **Ir2** are listed in Fig. 2. The melting points of **Ir1** and **Ir2** are 315 °C and 309 °C, respectively. From the TGA curves it can be observed that no loss of weight was observed below 360 °C, and the decomposition temperature (5% loss of weight) is 363 °C for **Ir1** and 368 °C for **Ir2**, indicating that the complexes are suitable for application in OLEDs.

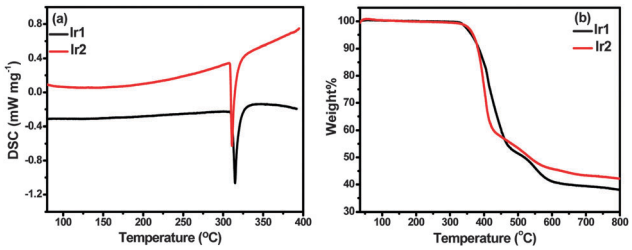

Fig. 2 The DSC and TGA curves of **Ir1** and **Ir2** complexes.

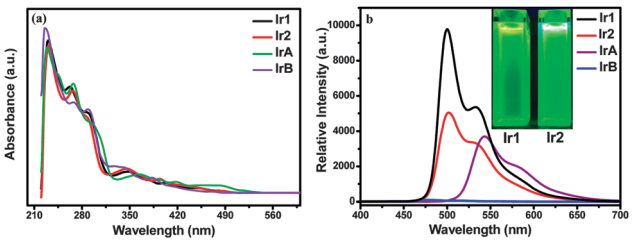

Fig. 3 The UV-vis absorption (a) and emission (b) spectra of complexes **Ir1**, **Ir2**, **IrA** and **IrB** in degassed dichloromethane (5×10^{-5} M) at room temperature.

Photophysical and electrochemical property

The UV-vis absorption and emission spectra of the two complexes **Ir1**, **Ir2** and the referring complexes **IrA**, **IrB** in CH_2Cl_2 (5×10^{-5} M) are shown in Fig. 3 and Fig. S4 (ESI†), and the photophysical data are collected in Table 1. The absorption spectra of these complexes show broad and intense bands below 320 nm, which can be assigned to the spin-allowed intraligand ^{1}LC ($\pi \rightarrow \pi^*$) transition of cyclometalated main ligands and tpip ligands. The weak bands last to 520 nm can be assigned to the spin-allowed metal-ligand charge transfer band (^{1}MLCT), partially overlapped by the broad LC absorptions, and spin forbidden ^{3}MLCT transition bands caused by the large spin orbital coupling (SOC) that was introduced by the iridium center, indicating an efficient spin–orbit coupling is a prerequisite for the phosphorescent emission. No distinct difference is observed in the absorption profiles for any of the complexes, indicating the similar electronic and vibrational structures of the ground states (S_0) and the first excited states (S_1).

For the phosphorescent emitters used in OLEDs, significant mixing of the lowest triplet and higher lying singlet excited states caused by the efficient SOC is in favor of high phosphorescent quantum efficiency. Moreover, strong SOC effect can drastically shorten the emission decay time and depress the triplet–triplet annihilation. The emission spectra in CH_2Cl_2 exhibit maximum peaks in the range of 500 nm to 502 nm generated from the electronic 0–0 transition between the lowest triplet excited state and the ground state, making them green phosphors. The emission at lower energy range around 533 nm might stem from the overlapping vibrational satellites.[8] In general, the emission bands from the MLCT states are broad and featureless, whereas a highly structured emission band mainly originates from the $^3\pi$–π^* state. Accordingly, all of the complexes emit from a mixture of MLCT states and the dominant ligand-based $^3\pi$–π^* state. This indicates that the MLCT characters involved in the emitting T_1 states of different complexes are various, but significant since a dominant MLCT character in T_1 usually leads to large inhomogeneity and low-energy lying metal-ligand vibrational satellites, smearing out the spectrum below the electronic original emission.[9]

Similar emission wavelength suggests that the position of the nitrogen atom of the pyridine and trifluoromethyl groups on the pyridine ring have no obvious effect on the wavelength of the Ir(III) complexes. Furthermore, the complexes based on bipyridine show much higher quantum efficiency (Φ_p) as 0.63 and 0.93 for **Ir1** and **Ir2** (Φ_p of **IrA** and **IrB** are only 0.06 and 0.10), respectively. These results indicate that the introduction of another pyridine in the main ligand will greatly improve the efficiency of iridium complexes and they have potential application in the OLEDs.

The redox properties and highest occupied molecular orbital (HOMO), lowest unoccupied molecular orbital (LUMO) energy levels of the dopants are relative to the charge transport ability and the OLED structure. To calculate the HOMO and LUMO energy levels of the heteroleptic complexes, cyclic voltammetry experiments of complexes **Ir1** and **Ir2** were carried out using ferrocene as the internal standard (Fig. 4). During the anodic scan in CH_2Cl_2, **Ir1** and **Ir2** exhibit a quasi-reversible redox with the oxidation potential in the region of 1.45–1.47 V, which is attributed to the metal-centered Ir^{III}/Ir^{IV} redox couple in accordance with the reported cyclometallated Ir(III) systems.[10] It is noteworthy that the complexes **Ir1** and **Ir2** show higher oxidation potentials than that of **IrA** and **IrB** (Table 1), which can be ascribed to the electronegative effect of the pyridine ring making the complexes more difficult to lose electron. The HOMO levels of the complexes were calculated from the oxidation potentials and the LUMO levels were calculated from the HOMO and band gap obtained from the UV-vis absorption

Table 1 Photophysical data of Ir(III) complexes **Ir1**, **Ir2**, **IrA** and **IrB**

Compound	T_m/T_d [a] (°C)	Absorption [b] λ (nm)	Emission λ_{em} [b] (nm) 298 K	$\tau_{298\ K}$ [b] (μs)	Φ_P [c] (%)	E_{ox} (V)	HOMO/LUMO [d] (eV)
Ir1	315/363	349/404/484	500/534	2.12	63	1.47	−5.93/−3.05
IrA	266/336	365/418/484/520	542/548	3.61	6	1.16	−5.82/−3.46
Ir2	309/368	346/394/486	502/533	3.13	93	1.45	−5.93/−3.04
IrB	334/358	342/383/471	480/487	1.83	10	1.26	−5.92/−3.29

[a] T_m: melting temperature, T_d: decomposed temperature. [b] Absorption, emission spectra and lifetime were taken in degassed CH_2Cl_2. [c] Φ: emission quantum yields were measured using the integrating-sphere system. [d] From the onset of oxidation potentials of the cyclovoltammetry (CV) diagram using ferrocene as the internal standard and the optical band gap from the absorption spectra in degassed CH_2Cl_2.

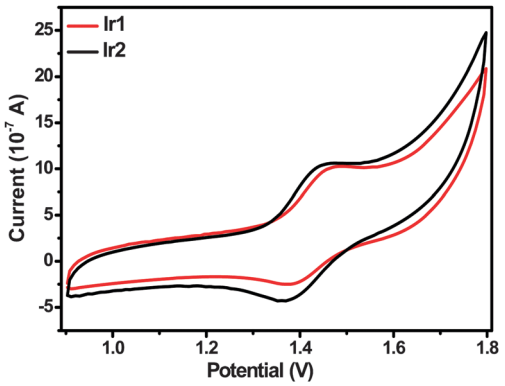

Fig. 4 Cyclic voltammograms of complexes **Ir1** and **Ir2**.

spectra (Table 1).[11] The HOMO levels of the two group complexes do not show much difference, while the LUMO levels of **Ir1** and **Ir2** complexes are much higher than that of the **IrA** and **IrB** ones, which would be helpful to the electron transport ability.

The density functional theory (DFT) calculations for Ir(III) complexes are conducted to gain insights into the electronic states and the orbital distribution employing the Gaussian09 software[12] with B3LYP functional.[13] The basis set used for C, H, N, O, F and P atoms was 6-31G(d,p), while the LanL2DZ basis set were employed for Ir atoms.[14] The solvent effect of CH_2Cl_2 was taken into consideration using a conductor like polarizable continuum model (C-PCM).[15] The relative energies of the HOMO/LUMO for all complexes are shown in Fig. 5 and the orbital distributions are summarized in Table S3 (ESI†). The results are helpful for the assignment of the electron transition characteristics and the discussion on the photophysical variations. For these complexes, the HOMOs correspond to a mixture of the phenyl or pyridine group attached to the pyridine ring (34.39–42.38%) and Ir d orbitals (51.73–56.39%) with minor contribution from the tpip ligand (5.89–9.22%), while the LUMOs are mainly localized on the main ligands (93.50–94.78%) with minor contribution from Ir d orbitals (3.08–3.74%) and tpip ligand (1.88–2.98%). Therefore, replacing the phenyl ring with the pyridine ring changes both the HOMO and the LUMO energy. Compared with the **IrA** and **IrB** complexes, the orbital distributions of HOMO for **Ir1** and **Ir2** have more contributions from Ir d orbitals and tpip ligand and less contribution from the bipyridine ligand. The calculation results indicated that the replacement of the phenyl group with pyridine affected the HOMO/LUMO levels of the iridium complexes.

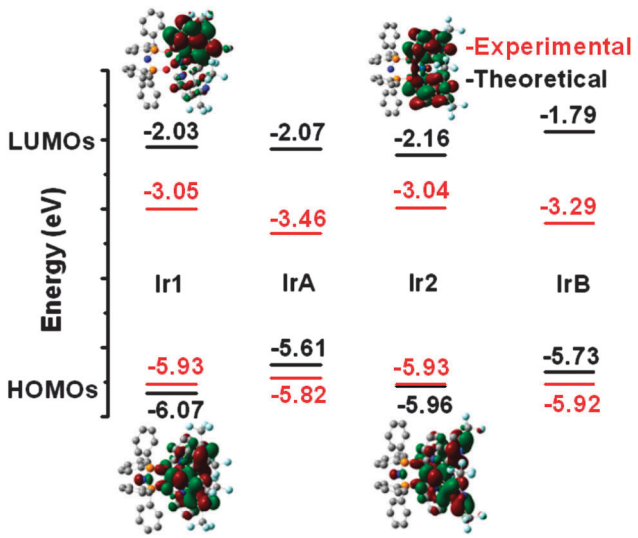

Fig. 5 Theoretical (black) and experimental (red, determined by cyclic voltammetry) HOMO/LUMO energy levels of complexes **Ir1**, **Ir2**, **IrA** and **IrB**.

Electron mobility

The good electron mobility of the phosphorescent emitters would facilitate the injection and transport of electrons, which will broaden the recombination zone, balance the distribution of hole–electron and reduce leakage current, leading to suppressed TTA and TPA effects,[16] improved recombination probability, high device efficiency, and low efficiency roll-off. To measure the electron mobility of the two complexes, we conducted the transient electroluminescence (TEL) measurement based on the device of ITO/TAPC (1,1-bis[4-[*N*,*N*-di(*p*-tolyl)amino]phenyl]cyclohexane, 50 nm)/Ir complexes (60 nm).[17] The TAPC is the hole-transport layer, whereas the Ir complexes perform as both the emissive and electron-transport layer. To check the accuracy of our measurements, we also measured the electron mobility of Alq_3 (tris-(8-hydroxyquinoline)aluminum, Fig. S, ESI†), which is the typically well-known electron transport material, whose electron mobility has been reported in many references.[18] The experimental results (Fig. 6, Fig. S, ESI†) showed that the electron mobilities in 60 nm **Ir1** and **Ir2** layers are between 7.00–7.20 $\times$ 10^{-6} cm^2 V^{-1} s^{-1} and 5.11–5.29 $\times$ 10^{-6} cm^2 V^{-1} s^{-1}, respectively, under an electric field from 1150 $(V\ cm^{-1})^{1/2}$ to 1300 $(V\ cm^{-1})^{1/2}$, while that of Alq_3 is between 4.74–4.86 $\times$ 10^{-6} cm^2 V^{-1} s^{-1}. The results suggest that **Ir1** and **Ir2** complexes have higher mobility than that of Alq_3 and **IrA**, **IrB**.[5c] In addition, the electron mobility of **Ir1** is better than that of **Ir2** suggesting that the N atom in the 5-position has higher effect on the improvement of the electron flow than in 4-position. The good electron transport ability of **Ir1** and **Ir2** will strengthen the recombination probability of electrons and holes, which indicate that OLEDs based on **Ir1** and **Ir2** may have good performances.

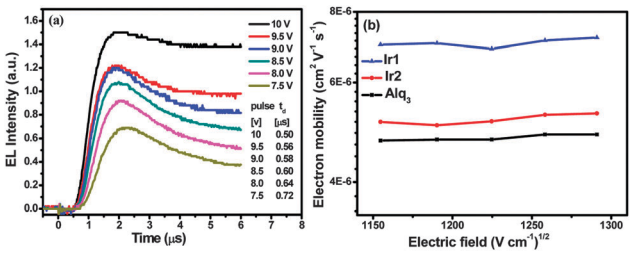

Fig. 6 (a) The transient EL signals for the device structure of ITO/TAPC (50 nm)/**Ir2** (60 nm) under different applied fields, and (b) electric field dependence of charge electron mobility in the thin films of **Ir1**, **Ir2** and Alq_3.

OLEDs performance

To verify our conjecture, devices **G1** and **G2** using **Ir1** and **Ir2** as the emitters, respectively, with the structure of ITO/TAPC (40 nm)/mCP (*N*,*N*′-dicarbazolyl-3,5-benzene, 10 nm)/Ir complex (8 wt%): PPO21 (3-(diphenylphosphoryl)-9-(4-(diphenylphosphoryl)phenyl)-9*H*-carbazole, 25 nm)/TmPyPB (1,3,5-tri(*m*-pyrid-3-yl-phenyl)benzene, 50 nm)/LiF (1 nm)/Al (100 nm) were investigated to evaluate the electroluminescence (EL) performances. Scheme 2 shows the energy level diagram of HOMO and LUMO levels (relative to vacuum level) for materials investigated in this study and their molecular structures. Because of the low HOMOs of **Ir1** and **Ir2** (−5.93 eV), we chose PPO21 (HOMO = 6.21 eV)[19] as the host material. mCP was also added as another hole transport material to lower the HOMO energy barrier between TAPC[20] and PPO21. TmPyPB[21] was used as an electron transport material.

The electroluminescence spectra, current density–luminance (*J*–*L*), current efficiency (η_c)–luminance (η_c–*L*) and external quantum efficiency–luminance (η_{EQE}–*L*) curves for **G1** and **G2** are shown in Fig. 7, voltage–luminance (*V*–*L*) and power efficiency–luminance (η_p–*L*) curves are list in Fig. S5 (ESI†), and the key EL data are summarized in Table 2. The optimal device performances are achieved at the doping level of 8 wt% and both the devices display excellent performances. All devices emit green light with the EL emission peaks at 505 and 506 nm for **G1** and **G2**, respectively, and the emission spectra are almost invariant of the current density and also do not show any concentration dependence. As shown in Fig. 7(a), the EL spectra are very close to the PL spectra of the complexes in CH_2Cl_2 solution, indicating that the EL emissions of the devices originate from the triplet excited states of the phosphors. No emission from TAPC, mCP and TmPyPB suggests that the exciton was only formed in the emissive layers. The absence of the PPO21 emission demonstrates that the energy and/or charge transfer from the host exciton to the phosphor is complete upon electrical excitation. The Commission Internationale de l'Eclairage (CIE) colour coordinates are $x = 0.32$, $y = 0.59$ for both **G1** and **G2** devices.

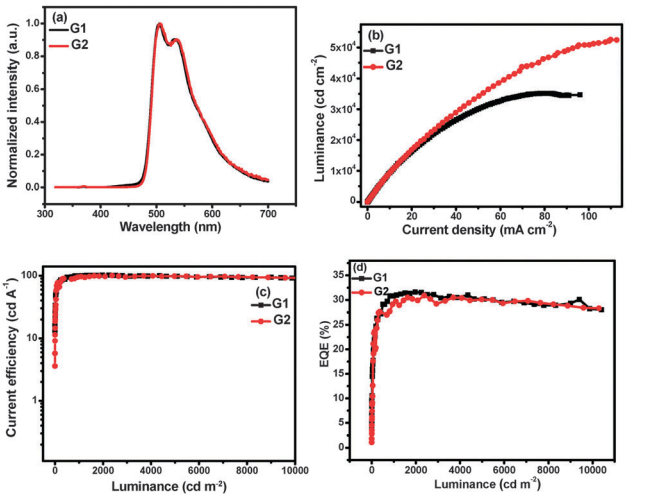

Fig. 7 Characteristics of devices of **G1** and **G2** with configuration ITO/TAPC (40 nm)/mCP (10 nm)/Ir complex (8 wt%): PPO21 (25 nm)/TmPyPB (50 nm)/LiF (1 nm)/Al (100 nm): (a) electroluminescence spectra; (b) current density–luminance (*J*–*L*) curves; (c) current efficiency–luminance (η_c–*L*) curves; (d) external quantum efficiency–luminance (η_{EQE}–*L*) curves.

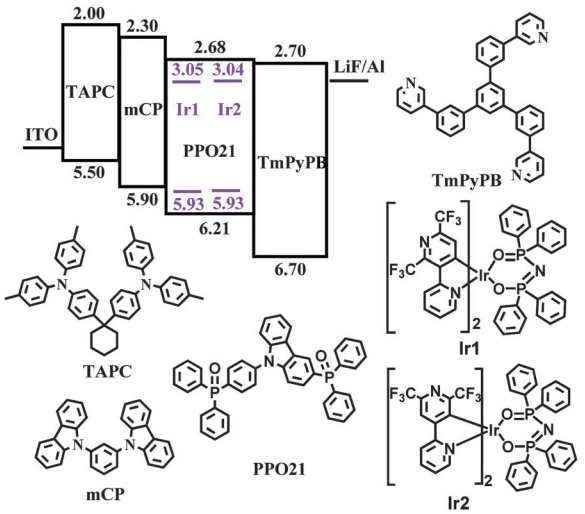

Scheme 2 Energy level diagram of HOMO and LUMO levels (relative to vacuum level) for materials investigated in this study and their molecular structures.

For device **G1**, the maximum current efficiency ($\eta_{c,max}$) is 101.96 cd A^{-1} obtained at 7.8 V with a maximum external quantum efficiency of 31.6%, the maximum power efficiency ($\eta_{p,max}$) is 43.34 lm W^{-1} (7.2 V) and the maximum luminance (L_{max}) is 35 178 cd m^{-2}. Device **G2** has a maximum luminance of 52 515 cd m^{-2} at 15.3 V and displays a maximum current efficiency of 99.97 cd A^{-1} with a maximum external quantum efficiency of 30.5%, and a maximum power efficiency of 43.60 lm W^{-1} (7.2 V). Furthermore, both the devices keep high efficiency at relative high luminance and the roll-off of EL efficiency is very low. For example, the current efficiencies for devices **G1** and **G2** still remain as high as 90.5 and 92.02 cd A^{-1} even at the brightness of 10 000 cd m^{-2}, which indicate that the complexes have application potential in OLEDs.

All the device performances are higher than that of **IrA** and **IrB** used as emitters. The high performances perhaps can be attributed to the high quantum efficiency, electron mobility of the Ir(III) complexes and suitable energy level. The small energy barrier (0.02 eV) between TmPyPB and PPO21 make it easy for electron injection. The low-lying HOMO level (6.7 eV) and high triplet energy level (2.78 eV) of TmPyPB will achieve a well confinement of hole within the emissive layer. Moreover, each material has high carrier mobility ($\mu_h = 1 \times 10^{-2}$ cm^2 V^{-1} s^{-1} for TAPC, $\mu_h = 5.0 \times 10^{-4}$ cm^2 V^{-1} s^{-1} for mCP and $\mu_e = 1 \times 10^{-3}$ cm^2 V^{-1} s^{-1} for TmPyPB).[19–21] The emitters even have higher electron mobility than that of Alq_3, which leads to a well-balanced charge carrier transport and efficient recombination. The dopants act as the hole and electron traps to retard the motion of both types of carriers. The good electron mobility of the dopants is particularly important for the reason that the hole mobility of the TAPC is higher than the electron mobility of the TmPyPB; moreover, the excitons accumulation is expected

Table 2 EL performances of the devices **G1** and **G2**

Device	Emitter	$V_{turn\text{-}on}$ [a] (V)	L_{max}(voltage)[b] [cd m^{-2} (V)]	$\eta_{c,max}$(voltage)[c] [cd A^{-1} (V)]	$\eta_{c,L10000}$ [d] (cd A^{-1})	$\eta_{EQE,max}$ (%)	$\eta_{p,max}$(voltage)[e] [lm W^{-1} (V)]	CIE (x,y)
G1	**Ir1**	4.1	35 178(17.4)	101.96(7.8)	90.52	31.6	43.34(7.2)	0.32, 0.59
G2	**Ir2**	4.9	52 515(15.3)	99.97(7.2)	92.02	30.5	43.60(7.2)	0.32, 0.59

[a] $V_{turn\text{-}on}$: turn-on voltage recorded at a luminance of 1 cd m^{-2}. [b] L_{max}: maximum luminance. [c] $\eta_{c,max}$: maximum current efficiency. [d] $\eta_{c,L10000}$: current efficiency at 10 000 cd m^{-2}. [e] $\eta_{p,max}$: maximum power efficiency.

in hole blocking layer near the interface of the emitting layer (Ir complexes: PPO21) and TmPyPB due to the high energy barrier between PPO21 and TmPyPB.[19–21] The accumulation of excitons is expected to cause the serious TTA and TPA of the iridium complexes, and consequently high efficiency roll-off. In our case, the good electron mobility of the phosphorescent emitters would improve the device efficiency and lower the efficiency roll-off.

It can also be observed that the turn on voltages of the two devices are high (4.1 V for **G1** and 4.9 V for **G2**) though the dopants have good electron mobility, and the charge transport of TAPC/TmPyPb are also high. One reason is that the carrier mobility of the host material PPO21 is very low ($\mu_h = 9 \times 10^{-6}$ cm^2 V^{-1} s^{-1} and $\mu_e = 3.0 \times 10^{-6}$ cm^2 V^{-1} s^{-1}).[19] Furthermore, the insertion of the mCP also would cause energy loss during the current flow. These two factors may lead to the high turn-on voltages of the devices.

Conclusions

In summary, using CF_3 substituted bipyridine as the main ligand and tpip as the ancillary ligand, we prepared two green phosphorescent iridium complexes (**Ir1** and **Ir2**). Compared with the phenylpyridine based complexes (**IrA** and **IrB**), the bipyridine contained complexes **Ir1** and **Ir2** show higher quantum efficiency and electron mobility. The OLEDs based on the **Ir1** and **Ir2** complexes (ITO/TAPC (40 nm)/mCP (10 nm)/Ir complex (8 wt%): PPO21 (25 nm)/TmPyPB (50 nm)/LiF (1 nm)/Al (100 nm)) show excellent performances with maximum current efficiencies of 101.96/99.97 cd A^{-1} and maximum external quantum efficiencies of 31.6% and 30.5% along with low efficiency roll-off. Even at the brightness of 10 000 cd m^{-2}, the current efficiencies still reach as high as 90.52 and 92.02 cd A^{-1}, suggesting that the improved electron mobility of the emitters would lead to a better carrier balance, and consequently to high efficiency with low efficiency roll-off.

Experimental

Materials and measurements

All reagents and chemicals were purchased from commercial sources and used without further purification. ^{1}H NMR spectra were measured on a Bruker AM 500 spectrometer. Mass spectra (MS) were obtained with an ESI-MS (LCQ Fleet, Thermo Fisher Scientific). High resolution mass spectra (Agilent 6540 UHD Accurate-Mass Q-TOF LC/MS) were recorded for the complexes. Absorption and photoluminescence spectra were measured on a UV-3100 spectrophotometer and a Hitachi F-4600 photoluminescence spectrophotometer, respectively. The decay lifetimes and absolute photoluminescent quantum yields were measured with an Edinburgh Instrument FLS-920 fluorescence spectrometer equipped with an integrating sphere in degassed CH_2Cl_2 solution at room temperature. Cyclic voltammetry measurements were conducted on a MPI-A multifunctional electrochemical and chemiluminescent system (Xi'an Remex Analytical Instrument Ltd Co., China) at room temperature with a polished Pt plate as the working electrode, platinum thread as the counter electrode and Ag–$AgNO_3$ (0.1 M) in CH_3CN as the reference electrode, tetra-*n*-butylammonium perchlorate (0.1 M) was used as the supporting electrolyte, using Fc^+/Fc as the internal standard, the scan rate was 0.1 V s^{-1}.

X-ray crystallography

X-ray crystallography of the single crystals of the complexes and ligand were carried out on a Bruker SMART CCD diffractometer using monochromated Mo Kα radiation (λ = 0.71073 Å) at room temperature. Cell parameters were retrieved using SMART software and refined using SAINT[22] on all observed reflections. Data were collected using a narrow-frame method with scan widths of 0.30° in ω and an exposure time of 10 s per frame. The highly redundant data sets were reduced using SAINT and corrected for Lorentz and polarization effects. Absorption corrections were applied using SADABS[23] supplied by Bruker. The structures were solved by direct methods and refined by full-matrix least-squares on F^2 using the program SHELXS-97.[24] The positions of metal atoms and their first coordination spheres were located from direct-methods E-maps; other non-hydrogen atoms were found in alternating difference Fourier syntheses and least-squares refinement cycles and during the final cycles refined anisotropically. Hydrogen atoms were placed in calculated position and refined as riding atoms with a uniform value of U_{iso}.

OLEDs fabrication and measurement

All OLEDs with the emission area of 0.1 cm^2 were fabricated on the pre-patterned ITO-coated glass substrate with a sheet resistance of 15 Ω sq^{-1}. All chemicals used for EL devices were sublimed in vacuum (2.2×10^{-4} Pa) prior to use. The deposition rate for organic compounds is 1–2 Å s^{-1}. The phosphor and PPO21 host were co-evaporated to form the 25 nm emitting layer from two separate sources. The cathode consisting of LiF/Al was deposited by the evaporation of LiF with a deposition rate of 0.1 Å s^{-1} and then by evaporation of Al metal with a rate of 3 Å s^{-1}. The effective area of the emitting diode is 0.1 cm^2. The characteristics of the devices were measured with a computer controlled KEITHLEY 2400 source meter with a calibrated silicon diode in air without device encapsulation. On the basis

of the uncorrected PL and EL spectra, the CIE coordinates were calculated using a test program of the spectra scan PR650 spectrophotometer.

Syntheses

All reactions were performed an under nitrogen atmosphere. Solvents were carefully dried and distilled from appropriate drying agents prior to use for the syntheses of ligands.

General syntheses of ligands. A stirred solution of 2,6-bis-(trifluoromethyl)pyridine (0.215 g, 10 mmol) in diethyl ether (20 mL) was cooled to −78 °C. LDA (lithium diisopropylamide, 6.0 mL, 10 mmol) was added over 20 min and stirred for 1 h, and then $B(OPr\text{-}i)_3$ (2.89 mL, 12.4 mmol) was added. The mixture was warmed to room temperature and stirred for another 1 h. The pH was adjusted to 10 by the slow addition of 10% aqueous NaOH solution (20 mL). After 1 hour, the organic phase was acidified to pH = 4 by the dropwise addition of 3 N HCl. The extraction with ethyl acetate and evaporation of the organic phase gave the crude corresponding aryl boronic acids. 2-Bromopyridine (1 mL, 10 mmol) and tetrakis(triphenylphosphine)palladium^0 (0.34 g, 0.3 mmol) and the boronic acids were added in 50 mL THF. After 20 mL of aqueous 2 N K_2CO_3 was delivered, the reaction mixture was heated at 70 °C for 1 day under an nitrogen atmosphere. The mixture was poured into water and extracted with CH_2Cl_2 (10 mL × 3 times). Finally, silica column purification (*n*-hexane : EtOAc = 7 : 1 as eluant) gave the colorless liquid 2′,6′-bis(trifluoromethyl)-2,3′-bipyridine (**L1**) and white solid 2′,6′-bis(trifluoromethyl)-2,4′-bipyridine (**L2**).

2′,6′-Bis(trifluoromethyl)-2,3′-bipyridine (L1). 10% yield. ^{1}H NMR (500 MHz, $CDCl_3$) δ 8.74 (d, J = 4.2 Hz, 1H), 8.14 (d, J = 8.0 Hz, 1H), 7.96 (d, J = 8.0 Hz, 1H), 7.85 (t, J = 7.2 Hz, 1H), 7.50 (d, J = 7.8 Hz, 1H), 7.46–7.38 (m, 1H). MS(ESI): Calcd: m/z 292.18 for $[M]^+$ ($C_{12}H_6F_6N_2$), found: m/z 293.25 $[M + H]^+$.

2′,6′-Bis(trifluoromethyl)-2,4′-bipyridine (L2). 30% yield. ^{1}H NMR (500 MHz, $CDCl_3$) δ 8.87–8.77 (m, 1H), 8.54 (s, 2H), 7.99–7.91 (m, 2H), 7.49 (ddd, J = 6.6, 4.7, 2.0 Hz, 1H). MS(ESI): Calcd: m/z 292.18 for $[M]^+$ ($C_{12}H_6F_6N_2$), found: m/z 293.33 $[M + H]^+$.

General syntheses of iridium complexes. A mixture of $IrCl_3 \cdot 3H_2O$ (1 mmol) and **L1** or **L2** (2.5 mmol) in 2-ethoxyethanol and water (20 mL, 3 : 1, v/v) was refluxed for 24 h. After cooling, the yellow solid precipitate was filtered to give the crude cyclometalated Ir(III) chloro-bridged dimer. Then, the slurry of crude chloro-bridged dimer (0.2 mmol) and Ktpip (0.5 mmol) in 2-ethoxyethanol (20 mL) was refluxed for 24 h. The solvent was evaporated at low pressure and the crude product was washed with water, and then chromatographed using CH_2Cl_2 to give complexes **Ir1** and **Ir2**, which were further purified by sublimation in vacuum.

Ir1. Yield: 40% ^{1}H NMR (500 MHz, $CDCl_3$) δ 9.09 (d, J = 5.6 Hz, 2H), 8.29 (d, J = 8.4 Hz, 2H), 7.79 (dd, J = 12.4, 7.7 Hz, 4H), 7.67 (t, J = 8.0 Hz, 2H), 7.39 (ddd, J = 19.9, 13.9, 7.5 Hz, 10H), 7.19 (t, J = 7.4 Hz, 2H), 7.01 (t, J = 6.7 Hz, 4H), 6.85 (t, J = 6.5 Hz, 2H), 6.36 (s, 2H). ESI-MS: 1192.67 $[M]^+$. HR EI-MS Calcd: m/z 1190.9295 for $[M]^+$ ($C_{48}H_{30}F_{12}IrN_5O_2P_2$), found: m/z 1192.1353 $[M + H]^+$.

Ir2. Yield: 59.7% ^{1}H NMR (500 MHz, CDCl3) δ 8.90 (d, J = 5.4 Hz, 1H), 7.94 (s, 1H), 7.77 (d, J = 8.0 Hz, 1H), 7.66 (dd, J = 11.9, 7.5 Hz, 2H), 7.53–7.31 (m, 4H), 7.27–7.13 (m, 3H), 7.08 (td, J = 7.6, 3.1 Hz, 2H), 6.66 (t, J = 6.5 Hz, 1H). ESI-MS: 1192.75 $[M]^+$ ($C_{48}H_{30}F_{12}IrN_5O_2P_2$). HR EI-MS Calcd: m/z 1190.9295 for $[M]^+$ ($C_{48}H_{30}F_{12}IrN_5O_2P_2$), found: m/z 1192.1364 $[M + H]^+$.

Acknowledgements

This study was supported by the National Natural Science Foundation of China (21371093, 91433113), the Major State Basic Research Development Program (2011CB808704, 2013CB922101) and the Natural Science Foundation of Jiangsu Province (BK20130054).

References

1 (*a*) S. Lamansky, P. Djurovich, D. Murphy, F. Abdel-Razzaq, H. E. Lee, C. Adachi, P. E. Burrow, S. R. Forrest and M. E. Thompson, *J. Am. Chem. Soc.*, 2001, **123**, 4304; (*b*) J. J. Kim, Y. You, Y. S. Park, J. J. Kim and S. Y. Park, *J. Mater. Chem.*, 2009, **19**, 8347; (*c*) Z. Q. Chen, Z. Q. Bian and C. H. Huang, *Adv. Mater.*, 2010, **22**, 1534; (*d*) S. M. Chen, G. P. Tan, W. Y. Wong and H. S. Kwok, *Adv. Funct. Mater.*, 2011, **21**, 3785; (*e*) J. M. Fernández-Hernández, C. H. Yang, J. I. Beltrán, V. Lemaur, F. Polo, R. Fröhlich, J. Cornil and L. D. Cola, *J. Am. Chem. Soc.*, 2011, **133**, 10543; (*f*) K. Y. Lu, H. H. Chou, C. H. Hsieh, Y. H. O. Yang, H. R. Tsai, H. Y. Tsai, L. C. Hsu, C. Y. Chen, I. C. Chen and C. H. Cheng, *Adv. Mater.*, 2011, **23**, 4933; (*g*) C.-H. Fan, P. Sun, T.-H. Su and C.-H. Cheng, *Adv. Mater.*, 2011, **23**, 2981; (*h*) S. Lee, S. O. Kim, H. Shin, H. J. Yun, K. Yang, S. K. Kwon, J. J. Kim and Y. H. Kim, *J. Am. Chem. Soc.*, 2013, **135**, 14321; (*i*) X. L. Yang, N. Sun, J. S. Dang, Z. Huang, C. L. Yao, X. B. Xu, C. L. Ho, G. J. Zhou, D. G. Ma, X. Zhao and W. Y. Wong, *J. Mater. Chem. C*, 2013, **1**, 3317; (*j*) H. Sasabe, H. Nakanishi, Y. Watanabe, S. Yano, M. Hirasawa, Y. J. Pu and J. Kido, *Adv. Funct. Mater.*, 2013, **23**, 5550; (*k*) H.-H. Chou, Y.-K. Li, Y.-H. Chen, C.-C. Chang, C.-Y. Liao and C.-H. Cheng, *ACS Appl. Mater. Interfaces*, 2013, **5**, 6168; (*l*) V. K. Rai, M. Nishiura, M. Takimoto and Z. Hou, *J. Mater. Chem. C*, 2014, **2**, 5317; (*m*) H. Cao, H. Sun, Y. Yin, X. Wen, G. Shan, Z. Su, R. n. Zhong, W. Xie, P. Li and D. Zhu, *J. Mater. Chem. C*, 2014, **2**, 2150; (*n*) A. Graf, P. Liehm, C. Murawski, S. Hofmann, K. Leo and M. C. Gather, *J. Mater. Chem. C*, 2014, **2**, 10298; (*o*) X. Xu, X. Yang, J. Dang, G. Zhou, Y. Wu, H. Li and W.-Y. Wong, *Chem. Commun.*, 2014, **50**, 2473; (*p*) X. Yang, G. Zhou and W.-Y. Wong, *J. Mater. Chem. C*, 2014, **2**, 1760.

2 W. S. Jeon, T. J. Park, S. Y. Kim, R. Pode, J. Jang and J. H. Kwon, *Appl. Phys. Lett.*, 2008, **93**, 063303.

3 (*a*) S. Heun and P. M. Borsenberger, *Chem. Phys.*, 1995, **200**, 245; (*b*) H. H. Fong, K. C. Lun and S. K. So, *Chem. Phys. Lett.*, 2002, **353**, 407.

4 (*a*) H.-H. Chou and C.-H. Cheng, *Adv. Mater.*, 2010, **22**, 2468; (*b*) S. O. Jeon, S. E. Jang, H. S. Son and J. Y. Lee, *Adv. Mater.*, 2011, **23**, 1436.

5 (*a*) Y. C. Zhu, L. Zhou, H. Y. Li, Q. L. Xu, M. Y. Teng, Y. X. Zheng, J. L. Zuo, H. J. Zhang and X. Z. You, *Adv. Mater.*, 2011, **23**, 4041; (*b*) M. Y. Teng, S. Zhang, S. W. Jiang, X. Yang, C. Lin, Y. X. Zheng, L. Y. Wang, D. Wu, J. L. Zuo and X. Z. You, *Appl. Phys. Lett.*, 2012, **100**, 073303; (*c*) Q. L. Xu, C. C. Wang, T. Y. Li, M. Y. Teng, S. Zhang, Y. M. Jing, X. Yang, W. N. Li, C. Lin, Y. X. Zheng, J. L. Zuo and X. Z. You, *Inorg. Chem.*, 2013, **52**, 4916; (*d*) H. Y. Li, L. Zhou, M. Y. Teng, Q. L. Xu, C. Lin, Y. X. Zheng, J. L. Zuo, H. J. Zhang and X. Z. You, *J. Mater. Chem. C*, 2013, **1**, 560; (*e*) C. C. Wang, Y. M. Jing, T. Y. Li, Q. L. Xu, S. Zhang, W. N. Li, Y. X. Zheng, J. L. Zuo, X. Z. You and X. Q. Wang, *Eur. J. Inorg. Chem.*, 2013, 5683; (*f*) M. Y. Teng, S. Zhang, Y. M. Jin, T. Y. Li, X. Liu, Q. L. Xu, C. Lin, Y. X. Zheng, L. Wang and J. L. Zuo, *Dyes Pigm.*, 2014, **10**, 105.

6 Y. T. Tao, C. L. Yang and J. G. Qin, *Chem. Soc. Rev.*, 2011, **40**, 2943.

7 L. J. Farrugia, *J. Appl. Crystallogr.*, 1997, **30**, 565.

8 A. F. Rausch, M. E. Thompson and H. Yersin, *Inorg. Chem.*, 2009, **48**, 1928.

9 (*a*) A. P. Wilde and R. J. Watts, *J. Phys. Chem.*, 1991, **95**, 622; (*b*) M. G. Colombo, T. C. Brunold, T. Riedener, H. U. Gudel, M. Fortsch and H. B. Burgi, *Inorg. Chem.*, 1994, **33**, 545.

10 S. Bettington, M. Tavasli, M. R. Bryce, A. Beeby, H. Al-Attar and A. P. Monkman, *Chem. – Eur. J.*, 2007, **13**, 1423.

11 (*a*) M. Thelakkat and H. W. Schmidt, *Adv. Mater.*, 1998, **10**, 219; (*b*) R. S. Ashraf, M. Shahid, E. Klemm, M. Al-Ibrahim and S. Sensfuss, *Macromol. Rapid Commun.*, 2006, **27**, 1454.

12 M. J. Frisch, G. W. Trucks, H. B. Schlegel, G. E. Scuseria, M. A. Robb, J. R. Cheeseman, G. Scalmani, V. Barone, B. Mennucci, G. A. Petersson, H. Nakatsuji, M. Caricato, X. Li, H. P. Hratchian, A. F. Izmaylov, J. Bloino, G. Zheng, J. L. Sonnenberg, M. Hada, M. Ehara, K. Toyota, R. Fukuda, J. Hasegawa, M. Ishida, T. Nakajima, Y. Honda, O. Kitao, H. Nakai, T. Vreven, J. A. Montgomery Jr., J. E. Peralta, F. Ogliaro, M. Bearpark, J. J. Heyd, E. Brothers, K. N. Kudin, V. N. Staroverov, R. Kobayashi, J. Normand, K. Raghavachari, A. Rendell, J. C. Burant, S. S. Iyengar, J. Tomasi, M. Cossi, N. Rega, J. M. Millam, M. Klene, J. E. Knox, J. B. Cross, V. Bakken, C. Adamo, J. Jaramillo, R. Gomperts, R. E. Stratmann, O. Yazyev, A. J. Austin, R. Cammi, C. Pomelli, J. W. Ochterski, R. L. Martin, K. Morokuma, V. G. Zakrzewski, G. A. Voth, P. Salvador, J. J. Dannenberg, S. Dapprich, A. D. Daniels, O. Farkas, J. B. Foresman, J. V. Ortiz, J. Cioslowski and D. J. Fox, *Gaussian 09, Revision A.01*, Gaussian, Inc., Wallingford, CT, 2009.

13 (*a*) C. T. Lee, W. T. Yang and R. G. Parr, *Phys. Rev. B: Condens. Matter Mater. Phys.*, 1988, **37**, 785; (*b*) A. D. Becke, *J. Chem. Phys.*, 1993, **98**, 5648; (*c*) P. J. Hay, *J. Phys. Chem. A*, 2002, **106**, 1634.

14 S. Chiodo, N. Russo and E. Sicilia, *J. Chem. Phys.*, 2006, **125**, 104107.

15 M. Cossi, N. Rega, G. Scalmani and V. Barone, *J. Comput. Chem.*, 2003, **24**, 669.

16 (*a*) J. Kalinowski, W. Stampor, J. Mezyk, M. Cocchi, D. Virgili, V. Fattori and P. Di Marco, *Phys. Rev. B: Condens. Matter Mater. Phys.*, 2002, **66**, 235321; (*b*) W. S. Jeon, T. J. Park, S. Y. Kim, R. Pode, J. Jang and J. H. Kwon, *Appl. Phys. Lett.*, 2008, **93**, 063303.

17 S. C. Tse, H. H. Fong and S. K. So, *J. Appl. Phys.*, 2003, **94**, 2033.

18 (*a*) H. Scher and E. W. Montroll, *Phys. Rev. B: Solid State*, 1975, **12**, 2455; (*b*) A. J. Pal, R. Osterbacka, K. M. Kallman and H. Stubb, *Appl. Phys. Lett.*, 1997, **71**, 228.

19 S. O. Jeon, K. S. Yook, C. W. Joo and J. Y. Lee, *Adv. Mater.*, 2010, **22**, 1872.

20 P. M. Borsenberger, L. Pautmeier, R. Richert and H. Bassler, *J. Chem. Phys.*, 1991, **94**, 8276.

21 S. J. Su, T. Chiba, T. Takeda and J. Kido, *Adv. Mater.*, 2008, **20**, 2125.

22 *SAINT-Plus, version 6.02*, Bruker Analytical X-ray System, Madison, WI, 1999.

23 G. M. Sheldrick, *SADABS An empirical absorption correction program*, Bruker Analytical X-ray Systems, Madison, WI, 1996.

24 G. M. Sheldrick, *SHELXTL-97*, Universität of Göttingen, Göttingen, Germany, 1997.